Remote Sensing of Environment
April 2014, Volume 146, Pages 159-171
http://dx.doi.org/ 10.1016/j.rse.2013.09.008

Errors in SMOS Sea Surface Salinity and their dependency on a priori wind speed

Xiaobin Yin[a], Jacqueline Boutin[a,*], Nicolas Martin[a], Paul Spurgeon[b], Jean-Luc Vergely[c], Fabienne Gaillard[d]

[a] LOCEAN/IPSL, UMR CNRS/UPMC/IRD/MNHN, France
[b] Argans, United Kingdom
[c] ACRI-ST, France
[d] IFREMER, LPO (CNRS-Ifremer-IRD-UBO), France

*: Corresponding author : Jacqueline Boutin

Abstract:

The wind speed (WS) provided by the European Centre for Medium-Range Weather Forecasts (ECMWF) is used to initialize the retrieval process of WS and Sea Surface Salinity (SSS) obtained by the Soil Moisture and Ocean Salinity (SMOS) mission. This process compensates for the lack of onboard instrument providing a measure of ocean surface WS independent of the L-band radiometer measurements. The SMOS-retrieved WS in the center of the swath (± 300 km) is adjusted regarding to its a priori estimate. The quality of the SMOS-retrieved SSS (SSS_{SMOS}) is better at the center of the swath than at the edge of the swatch because the larger number of brightness temperature measurements available at the center of the swath reduces the effects of noise and because the greater variety of incidence angles provides more scope for adjusting the WS. This highlights the advantage of using a multi-parameter retrieval with respect to a SSS-only retrieval in which the WS would be entirely prescribed. Systematic inconsistencies between the atmospheric WS modeled using ECMWF and the WS sensed by radiometers are observed. These inconsistencies in the WS are reduced by the retrieval scheme but they still lead to residual biases in the SSS_{SMOS}, especially in the eastern equatorial Pacific ocean if the ECMWF WS is used as an a priori estimate.

Highlights

► Multiangular SMOS TB allows adjusting wind speed in the center of the swath. ► The difference between SMOS and SSS_{ISAS} is lower in the center of the swath. ► SMOS SSS retrieved either using ECMWF or SSMIS wind speed as priors is compared. ► SMOS SSS biases and errors are decreased locally when SSMIS wind speed is used. ► Wind induced emissivity computed model differs from the remote sensed values.

Keywords : SMOS ; SSMIS ; ECMWF ; Wind speed ; Salinity

1. Introduction

The ocean is the dominant element of the global water cycle because 78% of the precipitation and 86% of the evaporation over the globe take place above the ocean and the river discharges flow from the land to the ocean (Schmitt, 2008). In addition, salinity and temperature determine the density of sea water so that salinity is a key parameter for studying the formation and circulation of water masses. Until recently it was only possible to measure the salinity in-situ. The recent development of sea surface salinity (SSS) observations with satellite L-band radiometers is one of the most promising tools to improve climate modeling and prediction. Two L-band satellite missions aimed at observing SSS from space have been launched in November 2009 (the European Soil Moisture and Ocean Salinity (SMOS) mission (Kerr et al., 2010)) and in June 2011 (the Aquarius mission (Le Vine et al., 2010)). The SSS can be measured in-situ over a practical salinity scale (pss hereafter), which corresponds to the conductivity ratio of a sea water sample to a standard potassium chloride solution (Unesco, 1981).

The SMOS satellite carries the L-band (1.4GHz) Microwave Imaging Radiometer with Aperture Synthesis (MIRAS) instrument, a microwave radiometer using interferometric technique for the first time on-board a satellite. It uses thinned arrays to achieve a moderate spatial resolution (~40 km) over a large swath. The MIRAS radiometer has a multi-angular imaging capability (Camps et al., 2005). The use of multi-angular brightness temperature (TB) allows for the reduction of the impact of radiometric noise on salinity retrievals. The global distribution of SSS retrieved from MIRAS TBs (SSS_{SMOS}) is qualitatively well sensed (Font et al., 2013; Reul et al., 2012). In particular, the latitudinal variations of the global SSS are well captured by SMOS (Yin et al., 2012a) and the SSS inter-annual variability in tropical regions detected by the Array for Real-Time Geostrophic Oceanography (ARGO) floats is consistent with the SSS_{SMOS} in the same region (Reul et al., 2013).

The sensitivity of sea surface TB to SSS increases with decreasing microwave frequency while the ground resolution of radiometer measurements decreases with decreasing microwave frequency. The L-band frequency range (1400–1427 MHz) has been chosen for the SMOS project because it features a significant sensitivity of radiometric measurements to changes in salinity and in soil moisture and it is protected against human-made emissions. However, even in this frequency range, the sensitivity of TB to SSS remains low. One main geophysical source of error in the retrieval of SSS from L-band TB comes from the uncertainty on the TB variation related to the surface roughness and foam. Actually, the wind effect on TB is equivalent to several pss in terms of retrieved SSS (Yueh et al., 2001). However, the sensitivity of L-band TB to wind speed (WS) and SSS varies differently with incidence angle θ for horizontal polarization (H-pol) and vertical polarization (V-pol) (Fig. 1). According to the Klein and Swift (1977) model, the sensitivity of TB to SSS (at 20 °C and 35 pss) ranges from -0.61 $K \cdot pss^{-1}$ to -0.45 $K \cdot pss^{-1}$ for H-pol and it ranges from -0.61 $K \cdot pss^{-1}$ to -0.79 $K \cdot pss^{-1}$ for V-pol, from 0° to 50° incidence angle. The sensitivity of TB to WS (at 10 ms^{-1}) derived from Yin et al. (2012b) model increases from 0.27 $K \cdot m^{-1}s$ to 0.31 $K \cdot m^{-1}s$ in H-pol and it decreases from 0.27 $K \cdot m^{-1}s$ to 0.18 $K \cdot m^{-1}s$ in V-pol, from 0° to 50° incidence angle.

The spatial variability featured on the global monthly SSS maps derived from in-situ measurements (Fig 2a, see Section 2.5 for a description) is quite well reproduced on monthly maps of SSS_{SMOS} retrieved using the European Centre for Medium-Range Weather Forecasts (ECMWF) WS (WS_{ECMWF} hereafter) as an *a priori* estimate ($rSSS_{ECMWF}$ hereafter) (Fig. 2b). There are however some differences in the open ocean far away from land and ice, for example in the eastern equatorial Pacific ocean where large positive biases appear and in the Southern Ocean at high latitude where negative biases appear (Fig. 2c). The aim

of this paper is to understand to what extent these differences can be explained by flaws in the WS_{ECMWF} or by some local features in surface roughness that are not well described by a wave spectrum for a fully developed sea such as the one used in the SMOS roughness model 1 (Yin et al. 2012b).

The SMOS-retrieved WS is compared with the Special Sensor Microwave Imager/Sounder (SSMIS) WS (WS_{SSMIS} hereafter) to analyze the ability of the SMOS retrieval process to adjust WS_{ECMWF} to the effective WS sensed by a microwave radiometer (called radiometric WS in the following). The accuracy of SSS_{SMOS} retrieved using WS_{SSMIS} as an *a priori* WS estimate (pWS) for initializing the retrieval process ($rSSS_{SSMIS}$ hereafter) is analyzed and it is compared with the one retrieved using WS_{ECMWF} as pWS. The ARGO SSS and monthly SSS maps derived from in-situ measurements are used as references. Data and methods are described in Section 2, results are presented in Section 3 and summarized and discussed in Section 4.

2. Data and Method

The analysis is performed in August 2010 and in September 2011 when large positive biases in SSS_{SMOS} occur and when the galactic noise impact on SMOS TB is relatively low.

2.1. SMOS Level 1C TB

MIRAS is a bidimensional interferometric radiometer with a Y-shaped antenna structure (Bayle et al., 2002; Camps et al., 2005). The field of view (FOV) of MIRAS contains both the Earth and the sky. Since the sky is a very stable and well-known target, both its direct contribution and the alias it induces can theoretically be estimated and removed (Anterrieu 2004; Camps et al., 2008). The resulting Extended Alias-Free FOV (EAFFOV) has the shape of a distorted hexagon. As a consequence, as the satellite moves ahead, any given point on the Earth is observed several times by numerous independent snapshots under various incidence angles along “dwell lines” parallel to the sub-satellite track (Waldteufel et al., 2003). The SMOS Level 1C ocean science measurement products (L1c) are generated by the European Space Agency (ESA) Data Processing Ground Station (DPGS) for each half-orbit. In the L1c product, 2D fields of the MIRAS TB reconstructed in the antenna polarization reference frame are projected onto an Earth-fixed grid known as the Icosahedral Snyder Equal Area (ISEA) grid (Snyder, 1992) and they are provided in the Earth geographical coordinates.

The data filtering configuration used here is the one used in the ESA SMOS Level 2 Ocean Salinity (L2OS) processor v5.50. The ISEA grid points on which ice is suspected to exist and the ISEA grid points located within 200 km from land are discarded. The measures of TB taken at the border of the EAFFOV or at the border of the unit circle replicas are filtered out. Then TBs that either have footprints with major axis larger than 100 km, lie in a region affected by Sun-point or Sun tails, are close to the specular direction of moon reflection, or are contaminated by high Sun glint and high galactic noise are filtered out. TBs detected as outliers or as Radio Frequency Interference (RFI) contaminated based on statistics along a dwell line are also filtered out. Detailed information about the flags is presented in Section 3 of the L2OS Algorithm Theoretical Baseline Document (ATBD) (http://www.argans.co.uk/smos/docs/deliverables/delivered/ATBD/SO-TN-ARG-GS-0007_L2OS-ATBD_v3.8_111117.pdf). For the TBs remaining after filtering, the incidence angle varies between 0° and 55° in the EAFFOV. However, the range of incidence angles used for WS and SSS retrievals varies depending on the distance of the dwell line with

respect to the center of the swath (Fig. 3a). The number of filtered TBs falling in a given ISEA grid point is larger than 150 within ± 300km from the center of the swath and it decreases toward the border of the swath (Fig. 3b).

The reprocessed MIRAS TBs produced by the up-to-date ESA SMOS level 1 operational processor v5.04 are used here. Some 436 ascending passes in August 2010 and 418 ascending passes in September 2011 are analyzed in order to minimize the uncertainties in simulated TB related to Faraday rotation and to galactic noise scattered by the ocean surface (Reul et al., 2008). For each ascending pass between 50°S to 15°N in August 2010 and September 2011, the estimate of the galactic noise scattered by the ocean surface is in the range of 2.0 K and 5.0 K for H-pol and in the range of 2.0 K and 3.0 K for V-pol. There can be an error of a few tenths of a Kelvin in these simulated values. For each ascending pass between 50°S to 15°N in August 2010 and September 2011, the Faraday rotation angle is in the range of -1.8° to 1.5° (the magnitude of its impact on TB averaged in the EAFFOV is within ±0.05 K). Moreover, much higher positive anomalies in the SSS_{SMOS} in the equatorial eastern Pacific Ocean occurred in August 2010 and September 2011 in comparison with other months.

2.2. Wind speed

The WS_{ECMWF} is the forecast from a semi-Lagrangian ECMWF operational model initialized with observations from surface, radio soundings, aircraft, and satellites. The WS_{ECMWF} is provided by the ECMWF Meteorological Archival and Retrieval System, which produces operational forecasts every three hours at a resolution of 0.225° × 0.225°. The WS at the lowest level of the 91 model levels is used, corresponding to an approximate 10 m height atmospheric WS (http://www.ecmwf.int/products/data/technical/model_levels/model_def_91.html). The WS_{ECMWF} used here is collocated with SMOS products and provided by DPGS.

The WS retrieval from microwave scatterometers and radiometers measurements neglects the air-sea stability. It is therefore convenient to derive u* from the atmospheric WS under the observed atmospheric conditions and to estimate a corresponding „equivalent neutral wind speed" (Liu and Tang, 1996) assuming that the atmosphere is neutrally stable and that the velocity of the sea surface current is equal to 0 ms^{-1}. The WS_{SSMIS} produced by Remote Sensing System (http://www.remss.com/) is used here. The WS_{SSMIS} is calibrated against buoy WS at 10 m height assuming a logarithmic wind profile (Wentz, 1997).

We collocate WS_{ECMWF} with WS_{SSMIS} from SSMIS F16 and F17. Daily 0.25° × 0.25° WS_{SSMIS} values flagged for large atmospheric water content and rain, or located within 50 km of rainy regions are not used in collocations. Collocation radii of ±0.5 hour and ±50 km referred to the MIRAS TB scanning time and location are used, and the nearest WS_{SSMIS} value is considered. In September 2011, WS_{SSMIS} from SSMIS F16 were not available. Hence, the number of collocations is much lower in September 2011 than in August 2010 in the Southern Ocean south of 40°S (Fig. 4).

The correlation coefficient between WSSSMIS and WSECMWF is 0.94 in August 2010 and 0.93 in September 2011 (Fig. 4, a and b). The standard deviation (std) of the differences between WSSSMIS and WSECMWF is 1.3 ms-1 in August 2010 and 1.1 ms-1 in September 2011 while the accuracy of WSSSMIS estimated by comparing it with buoy WS is higher than 1.4 ms-1 (Mears et al., 2001). WSSSMIS and WSECMWF are in good agreement up to 18 ms-1. Above 18 ms-1, WSSSMIS are higher than WSECMWF (Fig. 4, a and b). In the eastern part of the Pacific and Atlantic Ocean, WSECMWF are higher than WSSSMIS by

more than 2 ms-1 (as shown in the three black boxes in Fig. 4, c and d). Differences in these regions have already been documented (see Fig. 10 in (Atlas et al., 2011)) and are most likely due to persistent atmospheric or oceanic conditions affecting the microwave remote sensing of the ocean surface. In the eastern equatorial Pacific Ocean in particular, WSECMWF are higher than WSSSMIS by up to 3 ms-1. In the same region there is a strong westward surface current (see for instance Ocean Surface Current Analyses – Real time (OSCAR) product (http://www.oscar.noaa.gov/)).

Unlike a scatterometer signal which mainly relates to Bragg scattering by the ocean surface at a very specific wavelength, the roughness contribution to a radiometer signal results from a weighted average of the curvature wave spectrum over a broad range of wavelengths spanning gravity-capillarity and short gravity waves. The weights depend on the radiometer wavelength and on incidence angles (Johnson and Zhang, 1999; Dinnat, 2006). Wave spectra depend on the sea state, which is mainly influenced by factors such as present and past WS, surface currents, atmospheric stability, and swell. Hence there may not be a unique relationship between the atmospheric WS and the radiometric WS. However, the relationships with other sea state parameters are still poorly documented (Guimbard, 2010; Martin, 2013). Significant WS differences between the SSMIS observations and the ECMWF forecasts obtained using the atmospheric model are featured in the three black boxes shown in Fig. 4 and in the eastern equatorial Pacific ocean. These differences may be due to surface roughness modulation by intermediate wave breaking in the presence of a current (Johannessen et al., 2005), the contrasting structure of the mean square slope (MSS) field imposed by the large-scale patterns of the current field (Hansen et al., 2012) and the air-sea stability (Atlas et al., 2011).

2.3. Biases in the MIRAS TB

Despite substantial improvements in the SMOS instrument calibration and in the image reconstruction, systematic biases of several Kelvins in the FOV are still observed between averaged measured and simulated TBs. These bias patterns are currently estimated and mitigated using the Ocean Target Transformation (OTT) technique. They are computed using the mean spatial differences between measured and simulated TBs over a relatively homogeneous ocean area (Yin et al., 2012a) and they need to be removed before SSS retrievals are performed (Font et al., 2013).

Two sets of OTTs are computed either using WS_{ECMWF} and a roughness model fitted to WS_{ECMWF} (M1 in Yin et al., 2012b) or using WS_{SSMIS} and a roughness model fitted to WS_{SSMIS} (M3 in Yin et al., 2012b). The strategy and passes used by DPGS for computing the OTT are also used here. The passes and the validity time of OTTs for the L2OS processing can be found here (http://argans.co.uk/smos/docs/reports/SO-RP-ARG-GS-0068_L2OS-OTT_repro_v1.0_120112.pdf)

The strategy used for computing the OTT is summarized below. The SMOS L1c TB products over the eastern Pacific ocean located in the regions defined by the „parallelogram" (121°±16°W at 5°S, 111°±16°W at 45°S) and away from any island are used to compute the OTT. The Noise Injection Radiometers (NIR) are calibrated about every 2 weeks and the resulting parameters are introduced in the processing (Mecklenburg et al., 2012). Although the NIR calibrations are known to introduce small changes to TBs (0.5 K maximum over the ocean) (Oliva et al., 2013), it was decided that the OTT computations would be phased with NIR calibration events. During the period to be analyzed, five NIR calibration events were reported (Table 1). For each NIR calibration event, 10 ascending passes are used to

compute an ascending OTT. The typical time span for 10 selected passes is six to seven days.

Nominal criteria to select the 10 passes and the TB are:

1) if more than 10,000 ISEA grid points per pass fall inside the South Pacific ocean parallelogram region;

2) if the ISEA grid points are far from land and free of ice or rain contamination, if there is no missing ECMWF data or WS_{SSMIS}, if they are not flagged as having a high total electron content (TEC) gradient on the dwell line, if they have no L1c error flags set, and if WS at the ISEA grid point is between 3 and 12 ms^{-1};

3) if the TB measurements are validated according to L2OS ATBD.

Data below 3 ms^{-1} are rejected due to large discrepancies observed between SSS_{SMOS} and in-situ SSS (see for instance Fig. 8 in Yin et al., 2012b). These discrepancies are expected for several reasons. Sea surface roughness at low WS can be highly variable due to local WS, fetch, and duration of WS. Wave spectra are poorly known at low WS. Direct emissivity models of L-band TBs predict a jump (more than 1 K at 30° incidence angle) between a flat sea model and a rough sea model at 3 ms^{-1}. A strong dependence with WS below 3 ms^{-1} has been found using radiometric measurements. For example during the WInd and Salinity Experiment campaign, Etcheto et al. (2004) found a TB-to-WS dependency about 4 times larger for WS below 3 ms^{-1} than for WS above 3 ms^{-1}. A larger TB-to-WS dependency would lead to a larger error on retrieved SSS, assuming a constant error on WS.

If the filtering of one pass as described above discards more than 40% of TBs, the entire dataset obtained during this pass is discarded.

2.4. Retrievals with SMOS

The forward model implemented in the ESA L2OS processor simulates the flat sea emission with the Klein and Swift (1977) model and other contributions from the rough sea surface, the atmospheric emission and absorption (Liebe et al., 1993), and the scattering of galactic noise and of atmospheric radiation by the ocean surface. The forward model used to compute the TB at the top of the atmosphere without considering the Faraday rotation in the Earth reference frame can be expressed as

$$TB(\mathrm{SSS},\ \mathrm{SST},\ \mathrm{wind}) = \left(Tb_{flat} + Tb_{wind} + Tb_{DN}\Gamma + Tb_{gal\_ref}\right)e^{-\tau_{atm}} + Tb_{UP}, \qquad (1)$$

where Tb_{flat} is the brightness temperature for a flat sea, Tb_{wind} is the wind-induced contribution to sea surface TB, Tb_{DN} is the downward emitted atmospheric radiation, Γ is the sea surface reflection coefficient computed as 1-(Tb_{flat} + Tb_{wind})/SST, which takes into account the scattering by the ocean surface assuming that Tb_{DN} is homogeneous in all directions, Tb_{gal_ref} is the cosmic and galactic contribution already scattered by the sea surface taking into account the directional inhomogeneities of the galactic signal, Tb_{UP} is the upwelling atmospheric emission to the antenna and $e^{-\tau_{atm}}$ is the attenuation by the atmosphere.

Tb_{wind} is simulated by a roughness model and a foam model that have been tuned to fit a set of MIRAS TBs (Yin et al. 2012b). In the two-scale model (Yueh, 1997) sea surface is simulated as the superimposition of small waves on large waves, roughness scales being

partitioned into small and large scales by a cutoff wave number. The surface spectrum for a fully developed ocean is used whereas the effects of swell are neglected and the scattering by breaking waves is not considered.

The retrievals are based on the Levenberg and Marquardt iterative convergence method (Marquardt, 1963). The first guess geophysical inputs (SSS, SST, WS and TEC) are adjusted in order to minimize a "cost function" χ^2 expressed by

$$\chi^2 = \sum_{i=1}^{N} \frac{\left[TB_i^{meas} - TB_i^{mod}\right]^2}{\sigma_{TB_i}^2} + \sum_{j=1}^{Np} \frac{\left[P_j - P_j^{prior}\right]^2}{\sigma_{P_j}^2}, \qquad (2)$$

where *N* is the number of MIRAS TBs (TB_i^{meas}) available for the SSS retrieval at different incidence angles θ_i for the four Stokes parameters (TX, TY, T3 and T4) in the antenna frame as detailed in (Font et al., 2013; Yin et al., 2012a), TB_i^{mod} is the TB simulated at incidence angles θ_i, and $\sigma_{TB_i}^2$ is the expected variance of the differences between TB_i^{meas} and TB_i^{mod} given the instrumental radiometric resolution of MIRAS TBs and estimates of the model error. P_j are the retrieved parameters, in the case studied: SSS, SST, WS and TEC. P_j^{prior} is an *a priori* estimate of the P_j with an *a priori* variance $\sigma_{P_j}^2$. The value of $\sigma_{P_j}^2$ is representative of the reliability of P_j^{prior}: large $\sigma_{P_j}^2$ indicates that the estimate is not reliable, leading to very small weight within the total χ^2 minimization, and vice-versa.

The salinity used as an input for the inversion is taken from the monthly analysis of the World Ocean Atlas 2009 (WOA09) (Antonov et al., 2010). The SST and atmospheric parameters are forecasts provided by ECMWF. The first guess geophysical inputs (SSS, SST, WS, etc.) are adjusted by the retrieval process in order to minimize the quadratic sum of the differences between MIRAS TBs and TBs simulated by the forward model along a dwell line (Zine et al., 2008). In the operational L2OS iterative scheme, σSSS, σSST, σWS and σTEC are set to 100 pss, 1 °C, 2 ms-1 and 10 tecu, respectively.

The SSS and the WS are retrieved from MIRAS TBs (see Section 2.1) using the ESA L2OS v5.50 which uses the updated roughness model 1 (Yin et al., 2012b) and a new empirical galactic noise model fitted from MIRAS TBs (J. Tenerelli, pers. comm.). Five types of retrievals are considered here. The first retrieval is processed considering WS_{ECMWF} as pWS with σ_{WS} set to 2 ms^{-1} (it is the default configuration used at DPGS). The second one is processed with WS_{SSMIS} as pWS with σ_{WS} set to 2 ms^{-1}. The third and fourth ones are processed with σ_{WS} set to 5 ms^{-1} using WS_{ECMWF} and WS_{SSMIS} as pWS, respectively. The fifth one is processed without adjusting *a priori* WS_{ECMWF} during retrieval iterations (equivalent to setting σ_{WS} to 0 ms^{-1}). Notations of different types of retrieved SSS and WS are listed in Table 2. The first, the third, and the fifth datasets are processed using the roughness model M1 of Yin et al. (2012b) derived using WS_{ECMWF}. The second and the fourth datasets are processed using the roughness model M3 of Yin et al. (2012b) derived using WS_{SSMIS}. For each dataset the OTTs are computed using the corresponding WS used as pWS and roughness model respectively. Monthly averaged SSS maps at 0.5° × 0.5° resolution are constructed by considering a weighted average of SSS_{SMOS} as in Boutin et al. (2012) and smoothed based on the optimal interpolation method described in Gaillard et al. (2009).

2.5. In-situ SSS

Monthly reanalysis of SSS maps produced by the Laboratoire de Physique des Océans (http://wwz.ifremer.fr/lpo/SO-Argo/Products/Global-Ocean-T-S/Monthly-fields-2004-2010) are used. The monthly reanalysis of SSS maps (SSS_{ISAS}) is estimated using the In Situ Analysis System (ISAS) to produce gridded scalar fields based on the optimal interpolation method (Gaillard et al., 2009). This method constructs the SSS field as a linear combination of the anomaly relative to climatology and it is associated with a covariance matrix. In-situ SSS used in ISAS are taken from ARGO floats, Conductivity-Temperature-Depth Sensors from vessels, moorings of various projects and the Global Telecommunication System.

The SSS from ARGO floats (SSS_{ARGO}) in August 2010 and in September 2011 distributed in near real-time by the CORIOLIS data center (http://www.coriolis.eu.org) are also used. SSS_{SMOS} are collocated with SSS_{ARGO} using collocation radii of ±5 days and ±50 km. SSS_{ARGO} in six regions of the global ocean far away from land and ice are collected (Table 3).

The global $rSSS_{SSMIS}$ and the global $rSSS_{ECMWF}$ are analyzed by comparing them with SSS_{ISAS} and with SSS_{ARGO} in the six regions shown on Table 3.

3. Results

3.1. Wind speed retrieval

In the center of the swath the radiometric resolution is better, the range of incidence angle is larger, and the number of measurements is greater than away from the center of the swath. As a result, a higher quality of the retrieved parameters (SSS, WS and TEC) is expected based on simulations (Zine et al., 2008). The WS retrievals analyzed in this paper highlight the fact that WS_{ECMWF} are significantly corrected but only in the central part of the swath (about ± 300 km from the center) (Fig. 5) due to the multi-angular MIRAS TB availability. The differences between monthly averaged latitudinal profile of $rSSS_{ECMWF}$ and WOA09 SSS are smaller in the center of the swath (±300km) than in the border region of the swath (Fig. 6) partly because pWS are adjusted by the retrieval cost function with the multi-angular MIRAS TBs (Fig. 5b), and the SSS errors produced by pWS are thereby reduced.

3.2. Spatial variability of MIRAS TB related to wind speed: one pass study

In most cases, the observed latitudinal variations of TBs are consistent with the TB variations simulated using the forward model. However, discrepancies between the MIRAS TB and the simulated TB can arise if the WS_{ECMWF} and the WS_{SSMIS} are quite different. For example considering one pass over the eastern Pacific ocean on August 9th 2010, the WS_{ECMWF} and the WS_{SSMIS} are quite different around 17°S, where WS is low (Fig. 7, a to c). The MIRAS TBs averaged in the EAFFOV are also low in this region (Fig. 8, a and b). The TB simulated using the WS_{SSMIS} is about 0.5 K closer to the MIRAS TB than the one using WS_{ECMWF}, but still about 0.5 K higher than the MIRAS TB (Fig. 8, a and b). The retrieved WS are very close but 1 ms^{-1} lower than the WS_{SSMIS} independently from the choice of the WS_{SSMIS} or the WS_{ECMWF} as pWS (Fig. 7, d and e, and Fig. 8 c). This suggests that the SSMIS radiometric WS is closer to the MIRAS radiometric WS. Also, the differences between the retrieved WS using the WS_{ECMWF} as pWS (rWS_{ECMWF} thereafter) and the retrieved WS using the WS_{SSMIS} as pWS (rWS_{SSMIS} thereafter) are up to 2ms^{-1} (depending on locations) lower than the differences between WS_{ECMWF} and WS_{SSMIS} within ±300 km from

the center of the swath (Fig. 7, c and f), i.e. the SMOS retrieval converges to close retrieved WS, regardless of WS used as *a priori* estimates.

3.3. Monthly analysis of SMOS retrievals using different wind speeds as a priori estimates

The following analysis focuses on the center of the SMOS swath, which is where the retrieval significantly adjusts the WS.

In the eastern equatorial Pacific ocean, the $rSSS_{SSMIS}$ is 0.2 pss lower than the $rSSS_{ECMWF}$ (Fig. 9) and is similar to the SSS_{ISAS} (Fig. 10a). The rWS_{SSMIS} is similar to the WS_{SSMIS} while the rWS_{ECMWF} is 0.8 ms^{-1} lower than the WS_{ECMWF}, i.e. it is closer to the WS_{SSMIS} (Fig. 11). The SMOS retrieval is however not able to fully correct the differences between the WS_{SSMIS} and the WS_{ECMWF}. Compared with the SSS_{ISAS}, positive biases are stronger in the $rSSS_{ECMWF\_0}$ (see definition in Table 2) than those in the $rSSS_{ECMWF}$ and the $rSSS_{SSMIS}$, in the eastern equatorial Pacific (Fig. 2c and Fig. 10). Also, there are large negative biases in the $rSSS_{ECMWF\_0}$ near coasts and in the Southern ocean which is often roughened by high WS (Fig. 10b).

The $rSSS_{SSMIS}$ are lower than the $rSSS_{ECMWF}$ in the eastern part of the Pacific and Atlantic ocean (Fig. 9) where the WS_{SSMIS} are lower than the WS_{ECMWF} (see boxes in Fig. 4, c and d).

The statistics of the comparisons between the SSS_{SMOS} and the SSS_{ARGO} in the six regions defined in Table 3 are reported in Table 4. For the salinity retrievals taking place in August 2010, the mean (median) differences between the $rSSS_{SSMIS}$ and the $rSSS_{ECMWF}$ are close (within 0.09 (0.09) pss) in five out of the six regions except for the EEP region. In the EEP region, both the $rSSS_{SSMIS}$ and the $rSSS_{ECMWF}$ are significantly biased with respect to SSS_{ARGO} but the $rSSS_{SSMIS}$ is 0.21 pss closer to SSS_{ARGO} than $rSSS_{ECMWF}$ is (Table 4). Similar results are featured for the salinity retrievals taking place in September 2011 (Table 4). There are much less collocations in the SP and the SI regions in September 2011 than in August 2010 because F16 WS_{SSMIS} was not available. In the EEP region, the differences between the $rSSS_{SSMIS\_5}$ and the $rSSS_{ECMWF\_5}$ (see definitions in Table 2) decrease by about 0.1 pss with respect to the differences between the $rSSS_{SSMIS\_2}$ and the $rSSS_{ECMWF\_2}$ for the months of August 2010 and September 2011. This is due to the fact that the differences between the $rSSS_{ECMWF\_5}$ and the SSS_{ARGO} decrease by about 0.1 pss. However, the std of retrieved SSS increases by 13% to 44% (depending on the regions) if σ_{WS} is set to 5 ms^{-1}, in comparison with the std of retrieved SSS if σ_{WS} is set to 2 ms^{-1}.

In August 2010 and in September 2011, the std of the differences between the rWS_{SSMIS} and the rWS_{ECMWF} is lower than that between the WS_{SSMIS} and the WS_{ECMWF} in all six regions (Table 5). With increased σ_{WS}, the std of the differences between the rWS_{SSMIS_5} and the rWS_{ECMWF_5} (see definitions in Table 2) is even smaller in all six regions. The differences between the WS_{SSMIS} and the WS_{ECMWF} are adjusted by SMOS retrieval processes and the differences between the rWS_{SSMIS} and the rWS_{ECMWF} decrease significantly in the NSA and the EEP regions at the 95% level in comparison with the differences between WS_{SSMIS} and WS_{ECMWF}. However, the differences between the rWS_{SSMIS} and the rWS_{ECMWF} increase significantly at the 95% level in the SP region where WS is high. As for the SSS_{SMOS}, there are biases between the WS retrieved from MIRAS TBs and their pWS (WS_{SSMIS} and WS_{ECMWF}) close to the land (Fig. 2 c and Fig. 12).

No difference between the monthly averaged SST retrieved using WS_{SSMIS} as pWS and the SST retrieved using WS_{ECMWF} as pWS is found. Only ascending passes have been

considered for which TEC are very low (between 0 and 7 tecu), resulting in very small Faraday rotation angles between 0° and 1.5° during the two periods analyzed. The difference between the monthly averaged TEC retrieved with WS_{SSMIS} used as pWS and the TEC retrieved with WS_{ECMWF} used as pWS is less than 1 tecu, which can lead to a maximum difference of 0.02K in TB. Also, no correlations are observed between the differences in the retrieved SSS (WS) and in the retrieved TEC using two different WS as pWS.

4. Discussion and conclusion

Using multi-angular polarimetric MIRAS TBs, it is possible to adjust the WS in the center of the swath (within ±300km) by taking advantage of the different sensitivities of L-band H-pol and V-pol TBs to WS and SSS at various incidence angles. The differences between the SSS_{SMOS} and the SSS_{ISAS} are lower in the center of the swath (±300 km) than those at the border of the swath. In the center of the swath, the TBs involved in the retrieval scheme are more numerous, they have a better radiometric resolution, and they cover a larger incidence angle range which allows for a better adjustment of the *a priori* WS estimate. The inconsistencies between the WS_{ECMWF} and the radiometric WS_{SSMIS} are reduced in the center of the swath, and the std of the differences between the rWS_{SSMIS} and the rWS_{ECMWF} are lower than the std of the differences between the WS_{SSMIS} and the WS_{ECMWF}. This confirms that the SMOS operational retrieval scheme, even using very noisy TBs (with radiometric resolution of a single measurement ranging from 1.8 K to 5 K), successfully adjusts two different *a priori* WS estimates to closer values. It also reduces biases in the retrieved SSS with respect to a scheme that does not adjust WS during retrieval iterations.

The differences between the rWS_{SSMIS} and the rWS_{ECMWF} increase by 0.3 ms^{-1} in the Southern ocean at high latitudes. Yin et al. (2012b) noted large discrepancies between the wind-induced emissivity computed using the roughness model and that deduced from MIRAS TBs at low incidence angles located in the EAFFOV (see Fig. 6 in Yin et al. 2012). These large discrepancies are likely due to the correlation between latitudinal biases of MIRAS TBs and latitudinal distribution of mean WS which introduces errors in the empirically and the semi-empirically derived wind-induced emissivity (Yin et al., SMOS & AQUARIUS SCIENCE WORKSHOP 2013, http://www.congrexprojects.com/docs/default-source/13c07_docs2/dependence-of-smosmiras-brightness-temperatures-on-wind-speed-sea-surface-effect-and-latitudinal-biases_yin.zip). The discrepancies lead to reduced performance of the roughness model of Yin et al. (2012b) especially at high WS. The increased noise in SSS retrievals in cold waters also makes the WS retrieval noise larger. Given the large radiometric noise in MIRAS TBs, the modulation of wind direction in this roughness model is not well constrained. This could also lead to increased differences between the rWS_{SSMIS} and the rWS_{ECMWF}.

The differences between the WS_{SSMIS} and the WS_{ECMWF} are only partly adjusted by the SMOS retrieval scheme so that some wind-induced errors remain on the SSS_{ECMWF}. There are two possible reasons for these errors: 1) the ECMWF WS forecasts used as pWS may differ from the true meteorological WS, and 2) the wind-induced emissivity simulated with the ECMWF WS forecasts differs from the emissivity sensed by a microwave radiometer because the relationship between WS and the sea surface wave spectrum used in the emissivity model does not represent the true wave field. When the radiometric WS_{SSMIS} are used as pWS instead of the WS of ECMWF meteorological forecasts, SSS_{SMOS} biases and noises decrease locally since the SMOS sensed roughness is closer to the SSMIS-sensed roughness than to the roughness derived from WS_{ECMWF}. In order to analyze the reasons for the differences observed in the eastern equatorial Pacific ocean, the WS_{ECMWF} is compared

with the Tropical Atmosphere Ocean (TAO) mooring WS. The mean (std) difference between the WS_{ECMWF} and the TAO WS in the box 2°S2°N-140°W95°W in August 2010 is 0.1 (1.1) ms^{-1} while that between the WS_{SSMIS} and the TAO WS is 0.9 (1.3) ms^{-1}. The difference observed in this region is therefore likely related to sea surface effects such as the modulation of sea surface roughness by current-wave interactions and the air-sea stability. The altimeter observations highlight particularly well the errors in simulated MSS (Rascle and Ardhuin, 2013) as well as large biases in simulated wave heights in the eastern Pacific ocean associated with the dissipation of surface waves (Rascle et al., 2008). Note that the dissipation of surface waves was only slightly reduced in the latest ECMWF product (Bidlot et al., 2005). Similarly, the Cooperative Airborne Radiometer for Ocean and Land Studies (CAROLS) airborne data acquired by an L-band radiometer and a C-band scatterometer suggest that part of the L-band TB cannot be explained by WS but it can be related to MSS (A. Martin, personal comm.).

Positive SSS anomalies in the eastern equatorial Pacific ocean are not entirely removed when the WS_{SSMIS} is used as pWS. This could be due to the different sensitivity of emissivity and backscattering at various frequencies to the ocean wave field. As a result, the effective MSS estimated using data from radars operating at L-band, C-band, Ku-band and Ka-band are different (Guimbard, 2010).

Possible improvements in the SSS_{SMOS} can be made if another source of WS which is closer to the effective radiometric WS is used. However, not all MIRAS TBs can be collocated with the WS_{SSMIS}. This prevents the systematic use of the WS_{SSMIS} in the real-time processor. Increasing σ_{WS} to 5 ms^{-1} better removes systematic SSS biases but increases noise in the retrieved SSS. Future studies should concentrate on improving the roughness correction without increasing the noise in retrieved SSS.

Acknowledgments

We thank three anonymous reviewers for their very constructive comments. We also thank Joaquín Munoz-Sabater for his very helpful discussions about the ECMWF wind speed and Adrien Martin for fruitful discussions about roughness effects on L-band brightness temperature. This work was funded by the European Space Agency (ESA) expert support laboratory project and by the CNES/TOSCA/SMOS-GLOSCAL project. SSMIS data are produced by Remote Sensing Systems and sponsored by the NASA Earth Science MEaSUREs DISCOVER Project. The ARGO data are provided by CORIOLIS.

References

Anterrieu E. (2004). A resolving matrix approach for synthetic aperture imaging radiometers. *IEEE Transactions on Geoscience and Remote Sensing*, *42*(8), 1649-1656.

Antonov J., Seidov D., Boyer T., Locarnini R., Mishonov A., Garcia H., Baranova O., Zweng M., & Johnson D. (2010). World Ocean Atlas 2009, volume 2: salinity. In S. Levitus (Ed.), *NOAA Atlas NESDIS 69*. *U.S. Government Printing Office*. (pp. 1-40).

Atlas R., Hoffman R., Ardizzone J., M.Leidner S., Jusem J., Smith D., & Gombos D. (2011). A cross-calibrated, multiplatform ocean surface wind velocity product for meteorological and oceanographic applications. *Bulletin of the American Meteorological Society*, *92*(2), 157-174.

Bayle F., Wigneron J., Kerr Y., Waldteufel P., Anterrieu E., Orlhac J., Chanzy A., Marloie O., Bernardin M., Søbjærg S., Calvet J., Goutoule J., & Skou, N. (2002). Two-dimensional synthetic aperture images over a land surface scene. *IEEE Transactions on Geoscience and Remote Sensing*, *40*(3), 710-714.

Bidlot J., Abdalla S., & Janssen P. (2005). A revised formulation for ocean wave dissipation in CY25R1. *Tech. rep.*: Memo. R60.9/JB/0516, ECMWF, Reading, United Kingdom.

Boutin J., Martin N., Yin X., Font J., Reul N., & Spurgeon P. (2012). First assessment of SMOS data over open ocean: part II-sea surface salinity. *IEEE Transactions on Geoscience and Remote Sensing*, *50*(5, part 1), 1662-1675.

Camps A., Vall-llossera M., Duffo N., Torres F., & Corbella I. (2005). Performance of sea surface salinity and soil moisture retrieval algorithms with different auxiliary datasets in 2-D L-Band aperture synthesis interferometric radiometers. *IEEE Transactions on Geoscience and Remote Sensing*, *43*(5), 1189–1200.

Camps A., Vall-Llossera M., Corbella I., Duffo N., & Torres F. (2008). Improved image reconstruction algorithms for aperture synthesis radiometers. *IEEE Transactions on Geoscience and Remote Sensing*, *46*(1), 146–158.

Dinnat E. (2006). Correcting for roughness effect on L-band brightness temperature in the scope of sea surface salinity remote sensing: the active/passive synergy. *EWP 2303*, page 53. ESTEC/European Space Agency.

Etcheto J., Dinnat E., Boutin J., Camps A., Miller J., Contardo S., Wesson J., Font J., & Long D. (2004). Wind speed effect on L-band brightness temperature inferred from EuroSTARRS and WISE 2001 field experiments. *IEEE Transactions on Geoscience and Remote Sensing*, 42(10), 2206–2213.

Font J., Boutin J., Reul N., Spurgeon P., Ballabrera-Poy J., Chuprin A., GabarróC., Gourrion J., Hénocq C., Lavender S., Martin N., Martìnez J., Mcculloch M., Meirold-Mautner I., Mugerin C., Petitcolin F., Portabella M., Sabia R., Talone M., Tenerelli J., Turiel A., Vergely J., Waldteufel P., Yin X., Zine S., & Delwart S. (2013). SMOS first data analysis for ocean sea surface salinity determination. *International Journal of Remote Sensing*, 34(9-10), 3654-3670.

Gaillard F., Autret E., Thierry V., Galaup P., Coatanoan C., & Loubrieu T. (2009). Quality control of large Argo data sets. *Journal of Atmospheric and Oceanic Technology*, *26*(2), 337-351.

Guimbard S. (2010). Interprétation et modélisation de mesures à distance de la surface marine dans le domaine micro-onde. *Ph.D. dissertation, Université Versailles-Saint-Quentin-en-Yvelines*, Yvelines, France, 121 pp.

Hansen M., Kudryavtsev V., Chapron B., Johannessen J., Collard F., Dagestad K., Mouche A. (2012). Simulation of radar backscatter and Doppler shifts of wave-current interaction in the presence of strong tidal current. *Remote Sensing Of Environment*, *120*, 113-122.

Johannessen, J. , Kudryavtsev, V., Akimov, D., Eldevik, T., Winther, N., & Chapron, B. (2005). On radar imaging of current features: 2. Mesoscale eddy and current front detection. *Journal of Geophysical Research — Oceans*, *110*(C7), doi: 10.1029/2004JC002802.

Johnson J. & Zhang M. (1999). Theoretical study of the small slope approximation for ocean polarimetric thermal emission. *IEEE Transactions on Geoscience and Remote Sensing*, *37*(5), 2305–2316.

Kerr Y., Waldteufel P., Wigneron J., Cabot F., Boutin J., Escorihuela M., Font J., Reul N., Gruhier C., Juglea S., Delwart S., Drinkwater M., Hahne A., & Martín-Neira M. (2010). The SMOS mission: A new tool for monitoring key elements of the global water cycle. *Proc. IEEE*, *98*(5), 666-687.

Klein L. & Swift C. (1977). An improved model for the dielectric constant of sea water at microwave frequencies. IEEE Transaction on Antennas and Propagation, *AP-25*(1), 104–111.

Le Vine D., Lagerloef G., & Torrusio S. (2010). Aquarius and remote sensing of sea surface

salinity from space. *Proc. IEEE*, *98*(5), 688-703.
Liebe H., Hufford G., & Cotton M. (1993). Propagation modeling of moist air and suspended water/ice particles at frequencies below 1000 GHz. *Proc. NATO/AGARD Wave Propagation Panel, 52nd meeting, 3,* 1-10.
Liu W. & Tang W. (1996). Equivalent neutral wind. *Rep.*: Jet Propulsion Laboratory.
Marquardt D. (1963). An algorithm for least-squares estimation of non-linear parameters. *Journal of the Society for Industrial and Applied Mathematics*, *11*(2), 431–441.
Martin A. (2013). Analyse des mesures radiométriques en bande-L au-dessus de l"océan: campagnes CAROLS. *Ph.D. dissertation, Université Pierre et Marie Curie*, Paris, France, 172 pp.
Mears C., Smith D., & Wentz F. (2001). Comparison of SSM/I and buoy-measured wind speeds from 1987 – 1997. *Journal of Geophysical Research*, *106*(C6), 11719-11729.
Mecklenburg S., Drusch M., Kerr Y., Font J., Martín-Neira M., Delwart S., Buenadicha G., Reul N., Daganzo-Eusebio E., Oliva R., & Crapolicchio R. (2012). ESA"s Soil Moisture and Ocean Salinity mission: Mission performance and operations. *IEEE Transactions on Geoscience and Remote Sensing*, *50*(5, part 1), 1354-1366.
Oliva R., Martín-Neira M., Corbella I., Torres F., Kainulainen J., Tenerelli J., Cabot F., & Martin-Porqueras F. (2013). SMOS calibration and instrument performance after one year in orbit. *IEEE Transactions on Geoscience and Remote Sensing*, *51*(1), 654–670.
Rascle N., Ardhuin F., Queffeulou P., & Croizé-Fillonc D. (2008). A global wave parameter database for geophysical applications. Part 1: Wave-current–turbulence interaction parameters for the open ocean based on traditional parameterizations. *Ocean Modelling*, *25*(3-4), 154-171.
Rascle N. & Ardhuin F. (2013). A global wave parameter database for geophysical applications. Part 2: model validation with improved source term parameterization. *Ocean Modelling*, 70, 174-188..
Reul N., Fournier S., Boutin J., Hernandez O., Maes C., Chapron B., Alory G., Quilfen Y., Tenerelli J., Morisset S., Kerr Y., Mecklenburg S., & Delwart S. (2013). Sea surface salinity observations from space with the SMOS satellite: a new means to monitor the marine branch of the water cycle. *Surveys in Geophysics*, DOI: 10.1007/s10712-013-9244-0.
Reul N., Tenerelli J., Floury N., & Chapron B. (2008). Earth viewing L-band radiometer sensing of sea surface scattered celestial sky radiation. Part II: Application to SMOS. *IEEE Transactions on Geoscience and Remote Sensing*, *46*(3), 659–674.
Reul N., Tenerelli J., Boutin J. , Chapron B., Paul F., Brion E., Gaillard F., & Archer O. (2012). Overview of the first SMOS sea surface salinity products. Part I: Quality assessment for the second half of 2010. *IEEE Transactions on Geoscience and Remote Sensing*, *50*(5, part1), 1636-1647.
Schmitt R. (2008). Salinity and the global water cycle, *Oceanography*, *21*(1), 12-19.
Snyder J. (1992). An equal-area map projection for polyhedral globes. *Cartographica*, *29*(1), 10–21.
Tenerelli J., Reul N., Mouche A., & Chapron B. (2008). Earth-viewing L-band radiometer sensing of sea surface scattered celestial sky radiation - Part I: General characteristics. *IEEE Transactions on Geoscience and Remote Sensing*, *46*(3), 659–674.
Unesco (1981). Background papers and supporting data on the Practical Salinity Scale 1978. *Technical Papers in Marine Science*, *37*, 144 pp.
Waldteufel P., Boutin J., & Kerr Y. (2003). Selecting an optimal configuration for the Soil Moisture and Ocean Salinity Mission. *Radio Science*, *38*(3), 8051, doi: 101029/2002RS002744.
Wentz F., (1997). A well calibrated ocean algorithm for special sensor microwave/imager. Journal of Geophysical Research, *102*(C4), 8703–8718.
Yin X., Boutin J., & Spurgeon P. (2012a). First assessment of SMOS data over open ocean: part I Pacific Ocean. *IEEE Transactions on Geoscience and Remote Sensing*, *50*(5, part

1), 1648-1661.
Yin X., Boutin J., Martin N., & Spurgeon P. (2012b). Optimization of L-band sea surface emissivity models deduced from SMOS data. *IEEE Transactions on Geoscience and Remote Sensing*, *50*(5, part 1), 1414–1426.
Yueh S. (1997). Modeling of wind direction signals in polarimetric sea surface brightness temperatures. *IEEE Transactions on Geoscience and Remote Sensing*, *35*(6), 1400–1418.
Yueh S., West R., Wilson W., Li F., Njoku E., & Rahmat-Samii Y. (2001). Error sources and feasibility for microwave remote sensing of ocean surface salinity. *IEEE Transactions on Geoscience and Remote Sensing*, *39*(5), 1049–1060.
Zine S., Boutin J., Font J., Reul N., Waldteufel P., Gabarró C., Tenerelli J., Petitcolin F., Vergely J., Talone M., & Delwart S. (2008). Overview of the SMOS sea surface salinity prototype processor. IEEE Transactions on Geoscience and Remote Sensing, *46*(3), 621–645.

Tables

Table 1. NIR calibration events of SMOS

Event	Index	Time
NIR	1	2010-07-28, 02:20:00
NIR	2	2010-08-16, 15:10:00
NIR	3	2011-08-23, 15:28:37
NIR	4	2011-09-07, 16:00:00
NIR	5	2011-09-20, 15:56:00

Table 2. Notations and definitions of different Sea Surface Salinity (SSS) and Wind Speed (WS) used in this paper

Notation	Definition
SSS_{ISAS}	SSS estimated from in-situ data using In Situ Analysis System based on the optimal interpolation method
SSS_{ARGO}	SSS taken from ARGO floats
SSS_{SMOS}	SSS retrieved from MIRAS TBs
σ^2_{WS}	*A priori* variance on WS
$rSSS_{ECMWF}$	SSS retrieved from MIRAS TBs with ECMWF WS used as *a priori* estimate and σ_{WS} set to 2 ms^{-1}
$rSSS_{ECMWF\_0}$	SSS retrieved from MIRAS TBs with ECMWF WS used as *a priori* estimate without adjusting WS during retrieval iterations (equivalent to setting σ_{WS} to 0 ms^{-1})
$rSSS_{ECMWF\_5}$	SSS retrieved from MIRAS TBs with ECMWF WS used as *a priori* estimate and σ_{WS} set to 5 ms^{-1}
$rSSS_{SSMIS}$	SSS retrieved from MIRAS TBs with SSMIS WS used as *a priori* estimate and σ_{WS} set to 2 ms^{-1}
$rSSS_{SSMIS\_5}$	SSS retrieved from MIRAS TBs with SSMIS WS used as *a priori* estimate and σ_{WS} set to 5 ms^{-1}
pWS	WS used as *a priori* estimate for initializing retrievals
WS_{SSMIS}	SSMIS wind speed
WS_{ECMWF}	ECMWF wind speed
rWS_{ECMWF}	SSS retrieved from MIRAS TBs with ECMWF WS used as *a priori* estimate and σ_{WS} set to 2 ms^{-1}
rWS_{ECMWF_5}	SSS retrieved from MIRAS TBs with ECMWF WS used as *a priori* estimate and σ_{WS} set to 5 ms^{-1}
rWS_{SSMIS}	SSS retrieved from MIRAS TBs with SSMIS WS used as *a priori* estimate and σ_{WS} set to 2 ms^{-1}
rWS_{SSMIS_5}	SSS retrieved from MIRAS TBs with SSMIS WS used as *a priori* estimate and σ_{WS} set to 5 ms^{-1}

Table 3. Regions where the SSS_{SMOS} is collocated with the SSS_{ARGO}.

Zone	No. 1	No. 2	No. 3	No. 4	No. 5	No. 6
Full name	Southern Pacific ocean	Southern Indian ocean	Northern Tropical Pacific ocean	Northern Subtropical Atlantic ocean	Eastern Equatorial Pacific ocean	South-eastern Subtropical Pacific ocean
Acronym	SP	SI	NTP	NSA	EEP	SSP
Latitude	55S-40S	40S-20S	5N-15N	15N-30N	5S-1N	30S-10S
Longitude	180W-100W	110E-70E	180W-110W	45W-30W	130W-90W	130W-90W
SST (°C) Mean (std)	8.3 (2.2)	17.5 (3.4)	27.8 (0.5)	26.5 (0.8)	22.1 (1.6)	22.7 (2.0)
SSS (pss) Mean (std)	34.3 (0.2)	35.5 (0.3)	34.1 (0.4)	37.2 (0.3)	34.8 (0.22)	36.0 (0.3)

Table 4. Statistics of the SSS_{SMOS} collocated with the SSS_{ARGO} at ±5days and ±50km. SSS within ±300 km from the center of the track are used. Cases where the difference between two means is significant at the 95% level according to a t-test are shown in bold italic.

Zone	SP		SI		NTP		NSA		EEP		SSP	
August 2010												
No. of collocations	246		174		113		62		52		165	
a priori WS	SSMIS	ECMWF	SSMIS	ECMWF	SSMIS	ECMWF	SSMIS	ECMWF	SSMIS	ECMWF	SSMIS	ECMWF
σ_{WS}: 2 m s^{-1}												
mean(SSS_{SMOS}-SSS_{ARGO}) (pss)	-0.10	-0.17	-0.14	-0.05	-0.06	-0.14	-0.18	-0.21	***0.25***	***0.46***	-0.16	-0.13
median(SSS_{SMOS}-SSS_{ARGO}) (pss)	-0.08	-0.08	-0.14	-0.09	-0.03	-0.12	-0.12	-0.11	0.24	0.45	-0.18	-0.11
σ (SSS_{SMOS}-SSS_{ARGO}) (pss)	0.91	0.96	0.46	0.45	0.47	0.48	0.33	0.37	0.46	0.54	0.41	0.43
σ_{WS}: 5 m s^{-1}												
mean(SSS_{SMOS}-SSS_{ARGO}) (pss)	-0.14	-0.08	-0.08	-0.04	-0.06	-0.10	-0.09	-0.12	0.22	0.33	-0.16	-0.13
median(SSS_{SMOS}-SSS_{ARGO}) (pss)	-0.09	-0.08	-0.07	-0.03	-0.04	-0.09	-0.04	-0.09	0.28	0.34	-0.17	-0.15
σ (SSS_{SMOS}-SSS_{ARGO}) (pss)	1.31	1.29	0.62	0.58	0.54	0.54	0.51	0.53	0.57	0.57	0.58	0.58
September 2011												
No. of collocations	86		77		103		71		63		155	
σ_{WS}: 2 m s^{-1}												
mean(SSS_{SMOS}-SSS_{ARGO}) (pss)	-0.09	-0.23	-0.07	0.06	0.06	0.02	-0.12	-0.04	***0.22***	***0.49***	-0.01	0.07
median(SSS_{SMOS}-SSS_{ARGO}) (pss)	-0.20	-0.29	-0.05	0.02	0.08	-0.01	-0.09	-0.06	0.20	0.45	-0.02	0.08
σ (SSS_{SMOS}-SSS_{ARGO}) (pss)	0.87	0.91	0.57	0.62	0.41	0.43	0.40	0.39	0.45	0.54	0.37	0.38
σ_{WS}: 5 m s^{-1}												
mean(SSS_{SMOS}-SSS_{ARGO}) (pss)	-0.11	-0.14	-0.09	-0.06	0.06	0.01	-0.03	-0.05	0.26	0.38	-0.05	-0.03
median(SSS_{SMOSs}-SSS_{ARGO}) (pss)	-0.16	-0.17	-0.08	-0.09	0.10	0.00	0.05	0.01	0.22	0.31	-0.02	0.00
σ (SSS_{SMOS}-SSS_{ARGO}) (pss)	1.26	1.25	0.79	0.76	0.55	0.55	0.48	0.48	0.53	0.54	0.47	0.47

Table 5. Statistics of the differences between the WS_{SSMIS} and the WS_{ECMWF}, and statistics of the differences between the WS retrieved with one pWS and the WS retrieved with the other pWS. WS within ±300 km from the center of the track are used. Cases where the difference between means of (rWS_{SSMIS} - rWS_{ECMWF}) and (WS_{SSMIS} - WS_{ECMWF}) is significant at the 95% level according to a t-test are shown in bold italic. CI stands for confidence intervals.

Zone	SP			SI			NTP		
August 2010									
	WS_{SSMIS} – WS_{ECMWF}	rWS_{SSMIS} - rWS_{ECMWF}		WS_{SSMIS} – WS_{ECMWF}	rWS_{SSMIS} - rWS_{ECMWF}		WS_{SSMIS} – WS_{ECMWF}	rWS_{SSMIS} - rWS_{ECMWF}	
σ_{WS}		2m s^{-1}	5 m s^{-1}		2 m s^{-1}	5 m s^{-1}		2 m s^{-1}	5 m s^{-1}
mean (ms^{-1})	-0.28	***-0.54***	***-0.64***	-0.58	***-0.36***	***-0.46***	0.25	***0.11***	***-0.14***
median (ms^{-1})	-0.30	-0.55	-0.67	-0.57	-0.29	-0.48	0.25	0.20	-0.19
σ (ms^{-1})	0.80	0.57	0.42	0.80	0.57	0.43	1.02	0.85	0.52
95% CI σ (ms^{-1})	[0.77, 0.83]	[0.54, 0.59]	[0.40, 0.43]	[0.76, 0.85]	[0.54, 0.61]	[0.40, 0.45]	[0.97, 1.08]	[0.81, 0.90]	[0.49, 0.55]
September 2011									
mean (ms^{-1})	0.01	***-0.31***	***-0.59***	-0.41	-0.45	-0.34	0.08	0.08	***-0.23***
median (ms^{-1})	0.04	-0.34	-0.66	-0.42	-0.30	-0.42	0.00	0.07	-0.27
σ (ms^{-1})	1.09	0.69	0.50	1.28	1.00	0.46	1.02	0.64	0.50
95% CI σ (ms^{-1})	[1.05, 1.14]	[0.66, 0.72]	[0.47, 0.52]	[1.21, 1.36]	[0.94, 1.05]	[0.43, 0.48]	[0.97, 1.07]	[0.61, 0.67]	[0.47, 0.53]

Zone	NSA			EEP			SSP		
August 2010									
mean (ms^{-1})	-0.42	***-0.27***	***-0.16***	-1.38	***-0.70***	***-0.31***	-0.75	***-0.73***	***-0.66***
median (ms^{-1})	-0.49	-0.34	-0.17	-1.27	-0.58	-0.35	-0.78	-0.65	-0.73
σ (ms^{-1})	0.64	0.54	0.42	0.90	0.61	0.37	0.75	0.65	0.46
95% CI σ (ms^{-1})	[0.59, 0.70]	[0.50, 0.59]	[0.39, 0.46]	[0.83, 0.98]	[0.56, 0.67]	[0.34, 0.40]	[0.72, 0.79]	[0.62, 0.68]	[0.43, 0.48]
September 2011									
mean (ms^{-1})	-0.70	***-0.31***	***-0.25***	-1.43	***-0.66***	***-0.50***	-0.37	***-0.27***	***-0.47***
median (ms^{-1})	-0.69	-0.33	-0.30	-1.39	-0.65	-0.56	-0.42	-0.34	-0.54
σ (ms^{-1})	0.56	0.39	0.34	0.81	0.43	0.36	0.75	0.50	0.40
95% CI σ (ms^{-1})	[0.52, 0.62]	[0.36, 0.43]	[0.32, 0.38]	[0.74, 0.88]	[0.39, 0.47]	[0.33, 0.39]	[0.72, 0.79]	[0.48, 0.53]	[0.37, 0.43]

Figures

Fig. 1 Sensitivity of L-band TB to sea water salinity (top) and WS (bottom) as a function of incidence angle. These sensitivities are computed with the Klein and Swift (1977) permittivity model at 20 °C and 35 pss. The M1 model in Yin et al. (2012b) is used and WS is 10 ms^{-1} in the bottom panel.

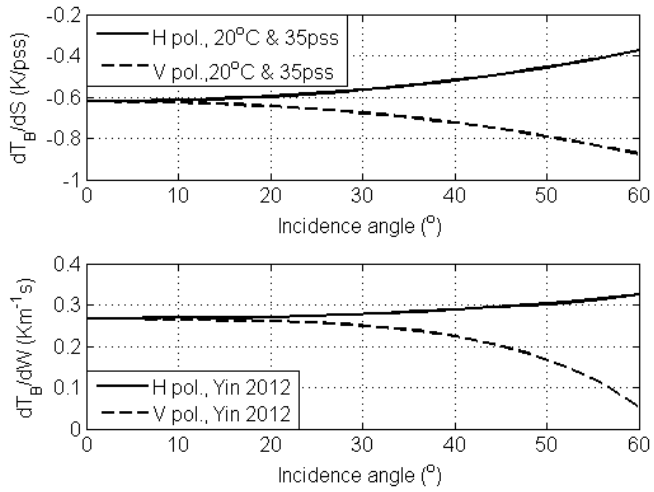

Fig. 2. Global maps of monthly SSS in August 2010 obtained from (a) SSS_{ISAS}, (b) $rSSS_{ECMWF}$, and (c) differences between $rSSS_{ECMWF}$ and SSS_{ISAS} maps. Only the $rSSS_{ECMWF}$ within ±300 km from the center of the swath are used.

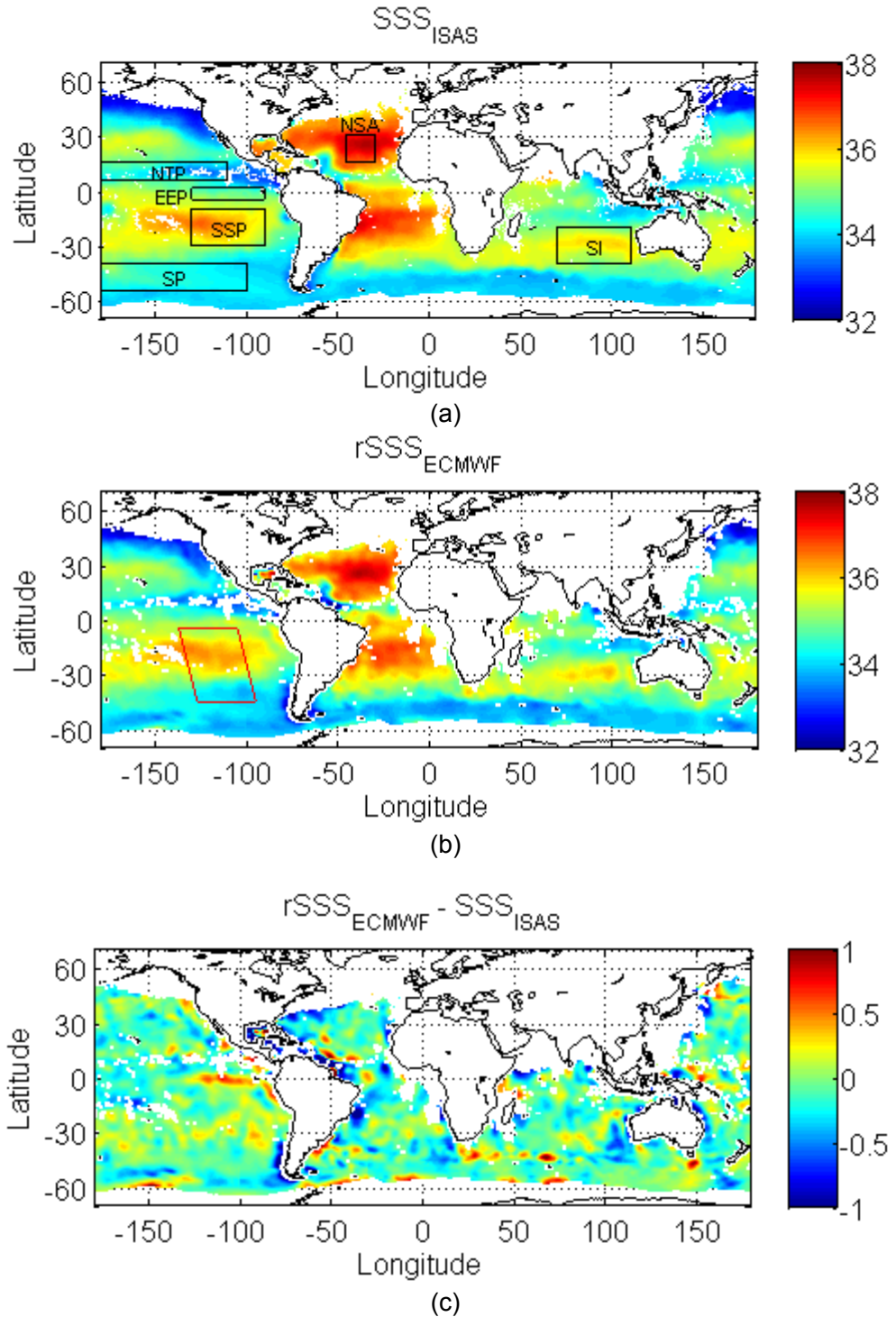

Fig. 3. (a) Variation of the incidence angle in the SMOS FOV and (b) number of filtered TBs falling in a given ISEA grid point as a function of the distance to the center of the swath. This example corresponds to an average of ISEA grid points from 45°S-5°S for the pass over the eastern Pacific ocean taken between 14:26:24 and 15:19:43 on 2010-08-09.

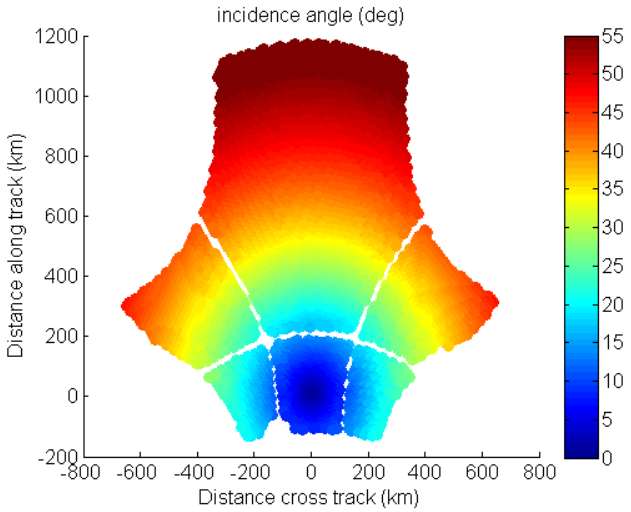

(a)

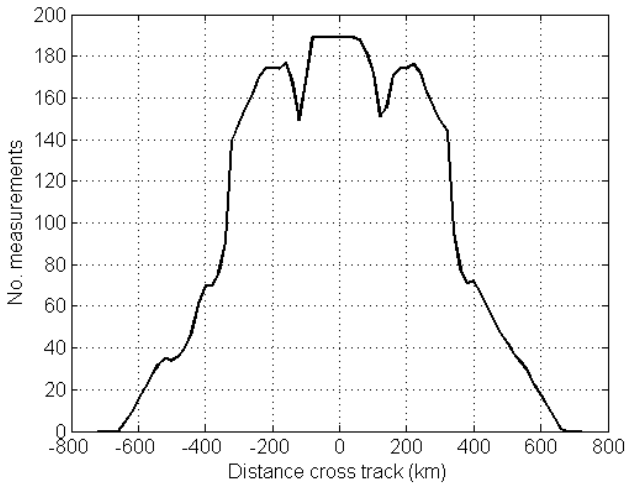

(b)

Fig. 4. Collocated WS_{SSMIS} versus WS_{ECMWF} in (a) August 2010, (b) September 2011, and monthly averaged global map of the differences between WS_{SSMIS} and WS_{ECMWF} in (c) August 2010 and (d) September 2011.

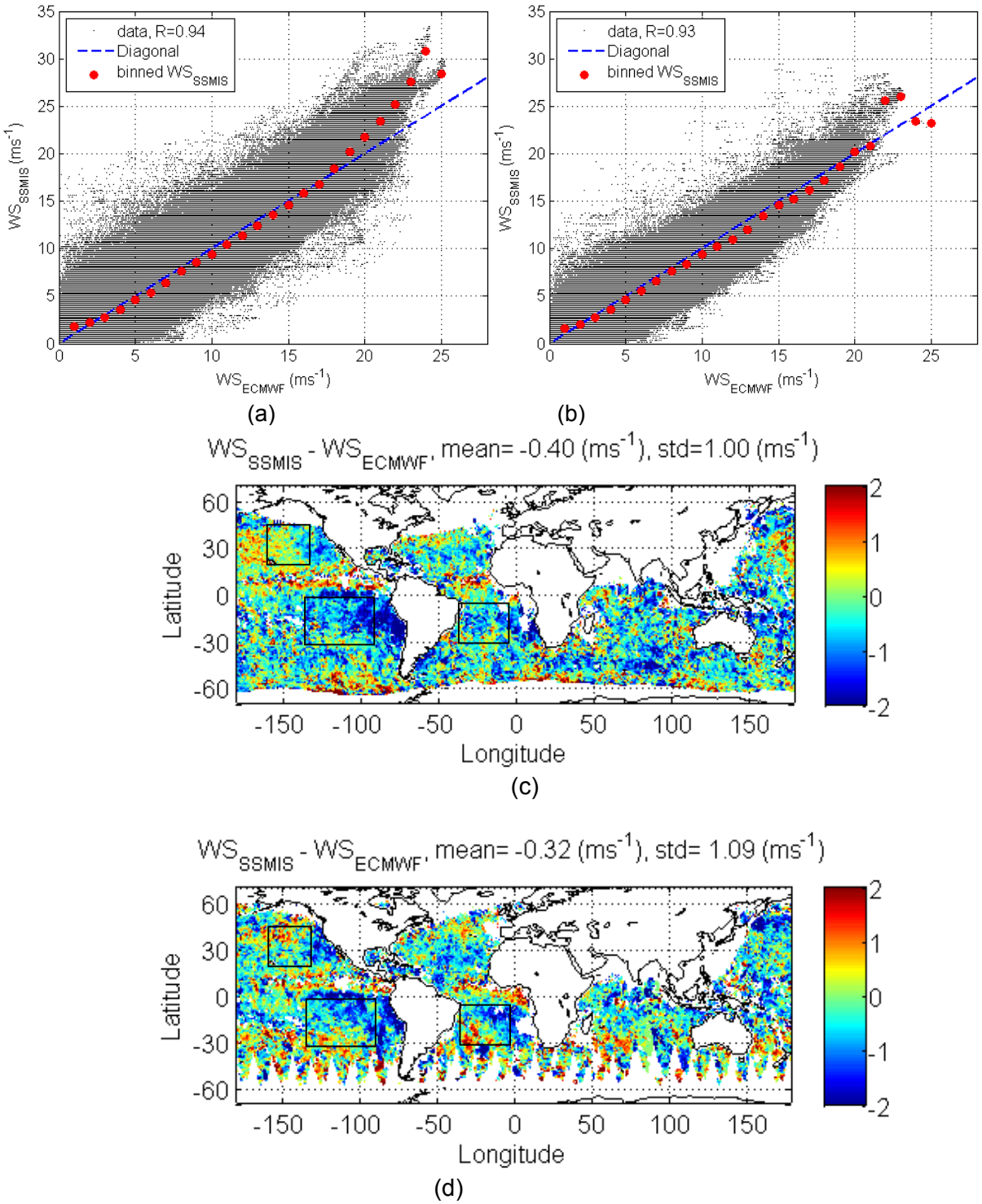

Fig. 5. (a) Monthly global averaged value of rWS_{ECMWF} minus WS_{ECMWF} versus distance to track and latitude in August 2010, and (b) monthly averaged latitudinal variations of rWS_{ECMWF} from south to north in August 2010, in the center of the swath (±300km) and away from the center of the swath.

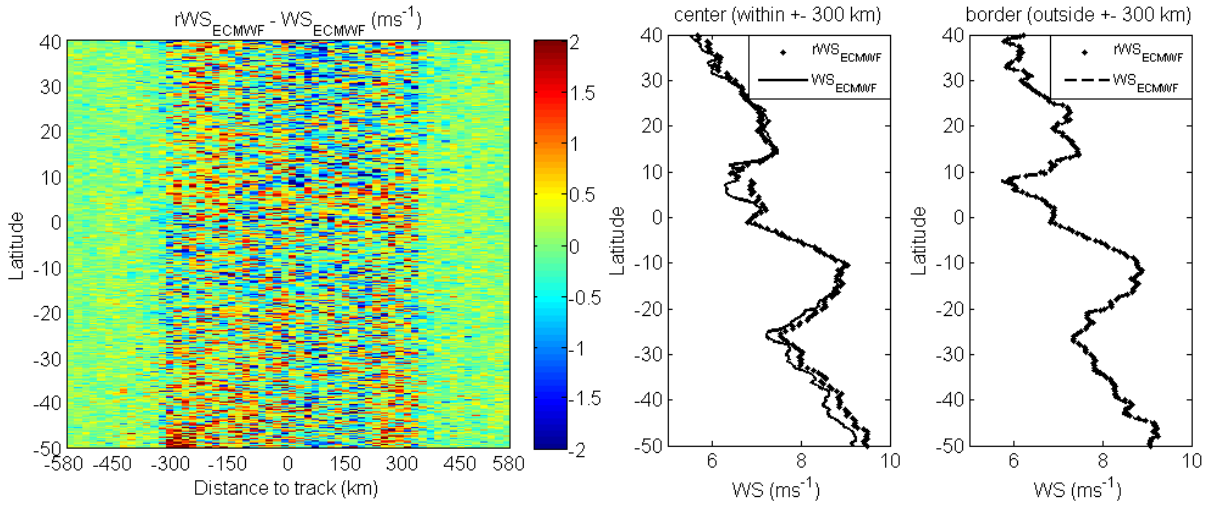

(a) (b)

Fig. 6. Monthly averaged latitudinal variations of $rSSS_{ECMWF}$ from south to north in August 2010 at ±300km from the swath (red) and outside of the center of the swath (blue). SSS are averaged over 140°W–100°W in longitude and over 0.5° bin in latitude. The WOA09 SSS is shown as references (black).

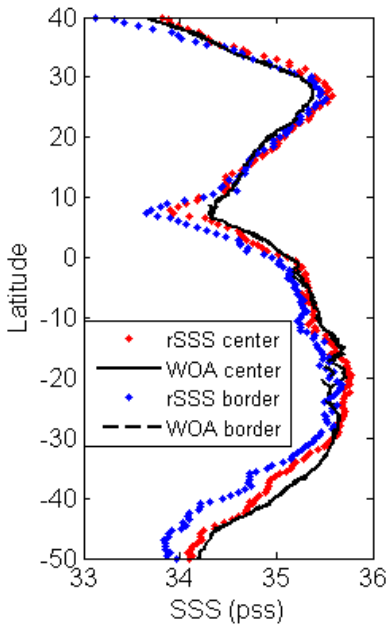

Fig. 7. (a) WS_{ECMWF}, (b) WS_{SSMIS}, (c) WS_{ECMWF} minus WS_{SSMIS}, (d) rWS_{ECMWF}, (e) rWS_{SSMIS} and (f) rWS_{ECMWF} minus rWS_{SSMIS} within ±300 km from the center of the swath for the same pass as the one in Fig. 3.

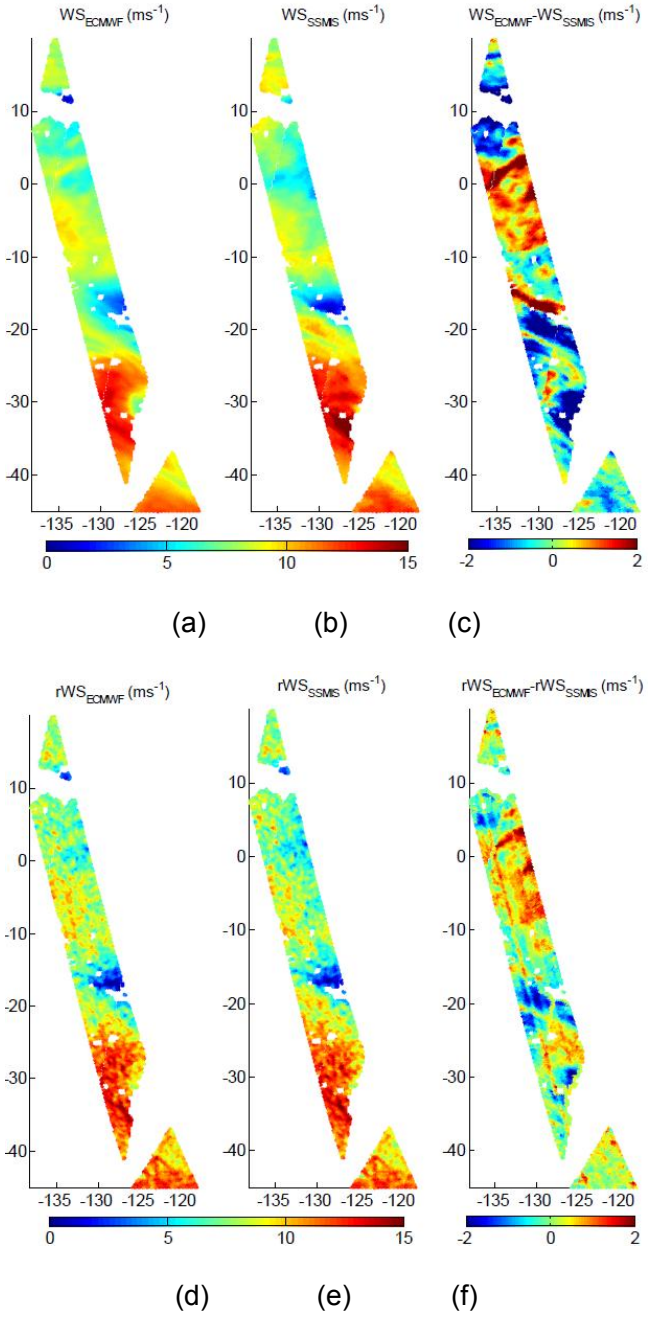

Fig. 8. Latitudinal profiles of the TBs averaged in the EAFFOV measured by MIRAS (black points) and simulated (red points) with WS_{ECMWF} (a) and with WS_{SSMIS} (b). The MIRAS TBs and their 5-point running mean are shown by black points and black line respectively. (c) Latitudinal profiles of WS_{ECMWF} (plain back line), WS_{SSMIS} (dashed black line), rWS_{ECMWF} (red points) and rWS_{SSMIS} (blue points). TBs and WS within ±300 km from the center of the swath are used. We show TB in X polarization that is the most sensitive to WS (as it is close to H-pol in the center of the swath). The pass is the same as the one in Fig. 3.

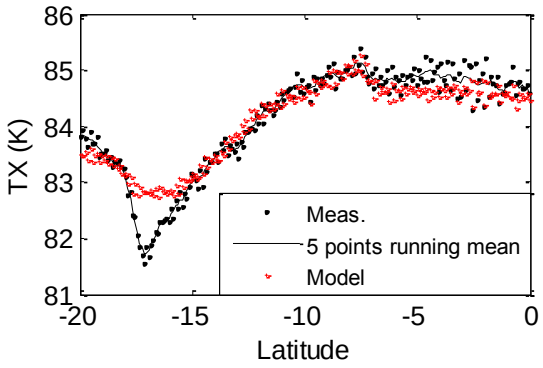

121

(a)

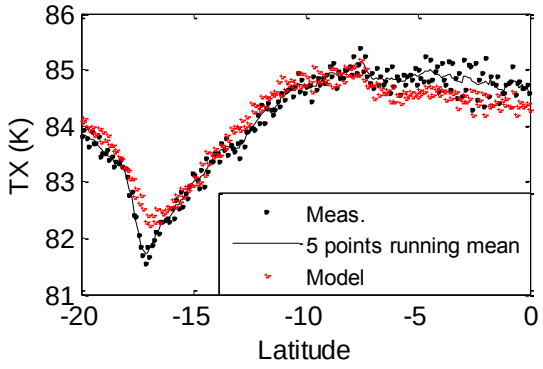

121

(b)

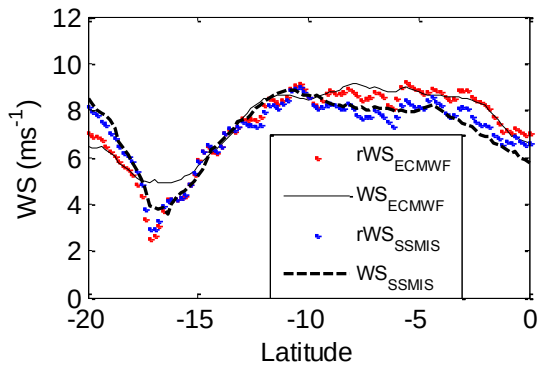

(c)

Fig. 9. Monthly maps of differences between SSS_{SSMIS} and SSS_{ECMWF} in (a) August 2010 and in (b) September 2011. Statistical distribution of $rSSS_{SSMIS}$ minus $rSSS_{ECMWF}$ in the eastern Pacific ocean for the EEP and the SSP regions defined in Table 3, in (c) August 2010 and in (d) September 2011. Only SSS within ±300 km from the center of the swath are used.

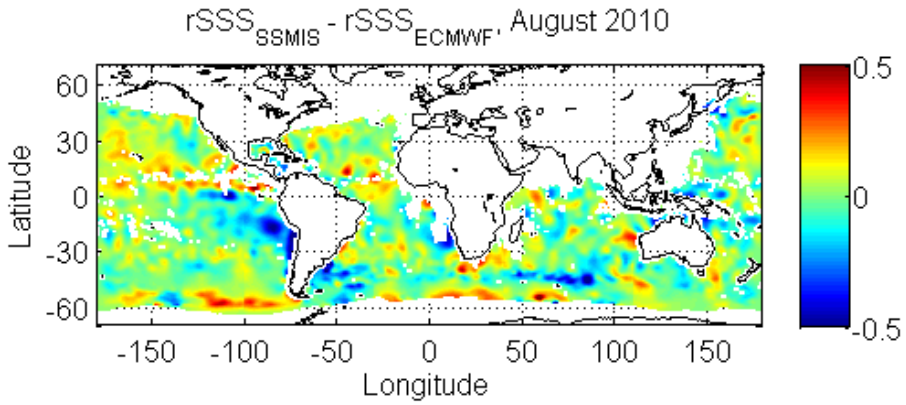

(a)

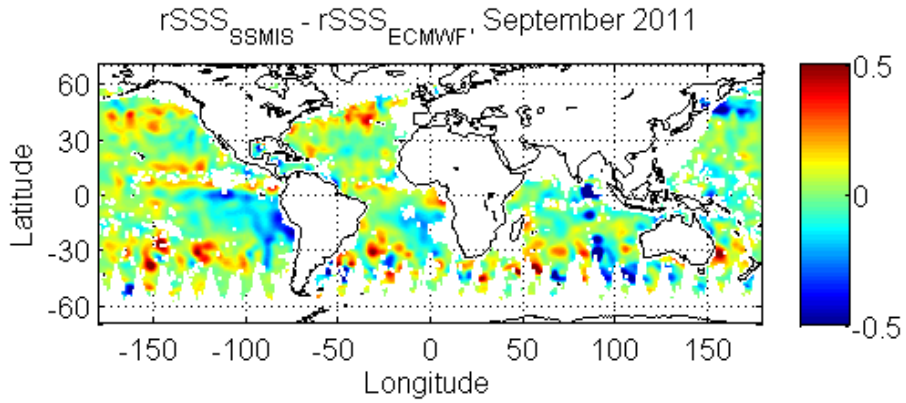

(b)

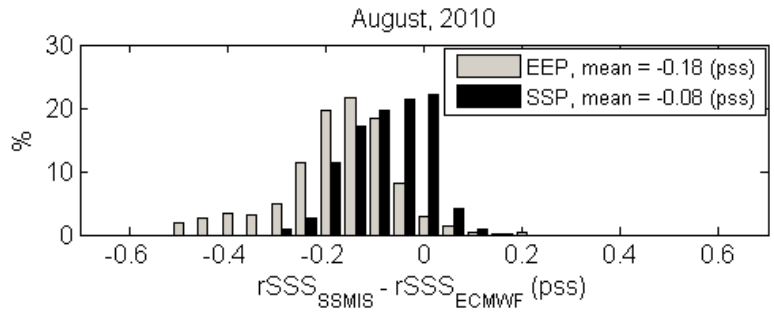

(c)

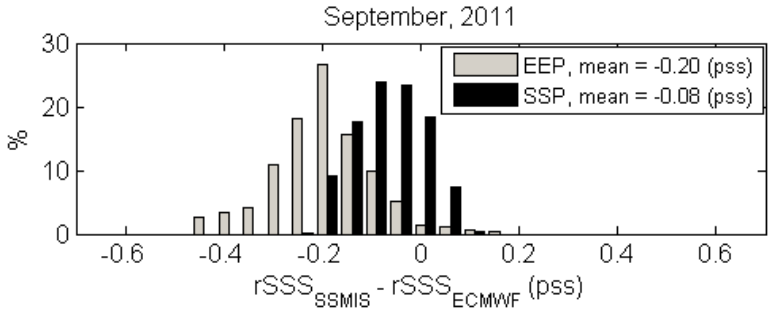

(d)

Fig. 10. (a) Monthly averaged maps of differences between $rSSS_{SSMIS}$ and SSS_{ISAS} in August 2010, and (b) differences between $rSSS_{ECMWF\_0}$ and SSS_{ISAS} maps in August 2010. Only SSS within ±300 km from the center of the swath are used.

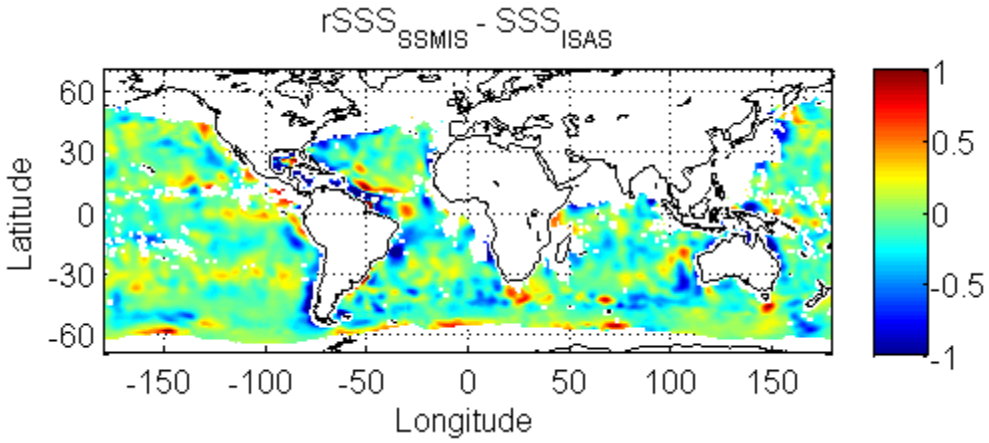

(a)

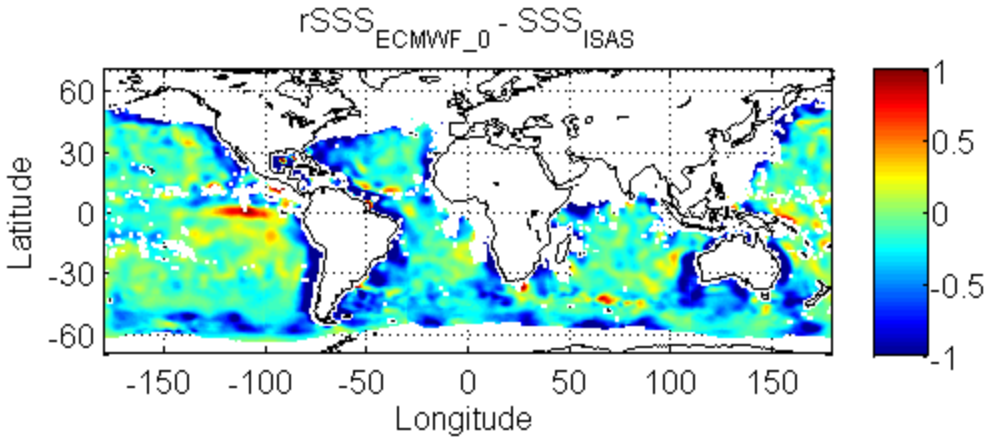

(b)

Fig. 11. Monthly maps of (a) rWS_{SSMIS}, (b) the differences between rWS_{SSMIS} and WS_{SSMIS}, (c) rWS_{ECMWF} and (d) the differences between rWS_{ECMWF} and WS_{ECMWF} in August 2010. Only WS within ±300 km from the center of the swath are used.

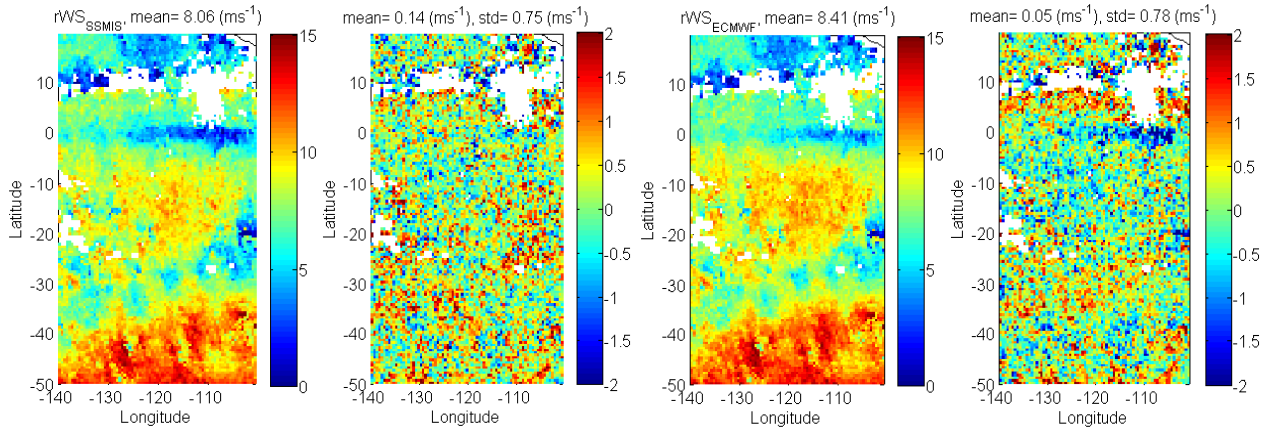

Fig. 12. Monthly maps of the differences between rWS_{SSMIS} and WS_{SSMIS} (top panels) and between rWS_{ECMWF} and WS_{ECMWF} (bottom panels) in August 2010 and September 2011. WS within ±300 km from the center of the swath are used.